

Studies of Reynolds Stress and the Turbulent Generation of Edge Poloidal Flows on the HL-2A Tokamak

T. Long¹, P. H. Diamond^{1,2*}, M. Xu^{1*}, R. Ke¹, L. Nie¹, B. Li¹, Z. H. Wang¹, J. Q. Xu¹, X. R. Duan¹ and HL-2A Team

¹ Southwestern Institute of Physics, Chengdu, China

² CASS and Dept. of Physics, University of California, San Diego, California, USA

E-mail: longt@swip.ac.cn

Abstract

Several new results on the physics linking edge poloidal flows to turbulent momentum transport are reported. These are based on experiments on the HL-2A tokamak. Significant deviation from the neoclassical prediction for mean poloidal flow in Ohmic and ECRH heated L mode discharges is derived from direct measurement of the turbulent Reynolds stress. The deviation increases prominently with ECRH heating power. The turbulent poloidal viscosity is synthesized from fluctuation data, and is found to be comparable to the turbulent particle diffusivity. The intrinsic poloidal torque characterized by the divergence of the non-diffusive residual stress is deduced from synthesis for the first time in a tokamak plasma. Experimental evidence which demonstrates the dynamics of spectral symmetry breaking in drift wave turbulence is in good agreement with the development of the poloidal torque. Taken together, these results elucidate the connections between power injection, turbulence development, pressure gradient and residual stress from symmetry breaking.

Keywords: tokamak, turbulent transport, poloidal flows, Langmuir probe

1. INTRODUCTION

Plasma poloidal mass flow and $E \times B$ flow are of great interest for their contributions to shear decorrelation of turbulence, and to the trigger mechanism for edge and core transport barriers formation [1, 2]. Experimental results on the DIII-D tokamak indicate a spin-up of main ion poloidal rotation at the transition from L mode to H mode. The transient increase in sheared poloidal flow and turbulent stress play critical roles in triggering the L-H transition[3]. Experimental evidences of sheared $E \times B$ flows linked to the location of rational surfaces show that $E \times B$ sheared flows driven by fluctuations can play an important role in the generation of transport barriers in the TJ-II stellarator [4]. The ion heat flux was demonstrated to govern the E_r well, which is responsible for the turbulence stabilization causing the L-H transition on the ASDEX-U tokamak [5, 6]. Experimental investigations on HL-2A tokamak indicate that, the increase of the mean $E \times B$ shear flow prior to the L-I and I-H transitions is

due to the ion diamagnetic component of radial electric field [7]. Indeed, the poloidal rotation term is at least as important as the pressure gradient term in the radial force balance relation which determines radial electric field, i.e. $E_r = \nabla_r P_i / (Z_i e n_i) - v_{\theta i} B_\phi + v_{\phi i} B_\theta$ [8]. A large excursion in the poloidal rotation of carbon impurity ions relative to the neoclassical prediction was associated with internal transport barrier formation in TFTR reversed shear plasmas [9]. Well-established neoclassical models [10-13] have been used to calculate the poloidal rotation velocity. Based on these, a significant deviation of poloidal rotation from the neoclassical prediction was observed in previous studies on many tokamaks [14-17].

The theory of turbulence effects on mean poloidal flow via turbulent flux of momentum--Reynolds stress--has been widely studied in the fusion community [18-25], since it was first proposed in 1990s. The divergence of the Reynolds stress $\langle \tilde{v}_r \tilde{v}_\theta \rangle$ shifts the poloidal flow from the neoclassical value [26]. This normally requires inhomogeneous turbulence and is consistent with momentum balance. Considering the case of a stationary flow, $\langle v_\theta \rangle$ is given by:

$$\mu_{ii}^{(neo)} (\langle v_\theta \rangle - \langle v_\theta \rangle_{neo}) = -\partial_r \langle \tilde{v}_r \tilde{v}_\theta \rangle. \quad (1)$$

Here, $\mu_{ii}^{(neo)}$ is the neoclassical viscosity coefficient (i.e. the flow damping rate), $\langle v_\theta \rangle$ denotes poloidal rotation and $\langle v_\theta \rangle_{neo}$ represents neoclassical poloidal rotation. The Reynolds stress can be expressed in the form [27, 28]:

$$\langle \tilde{v}_r \tilde{v}_\theta \rangle = -\chi_\theta \frac{\partial \langle v_\theta \rangle}{\partial r} + v_r^{eff} \langle v_\theta \rangle + \Pi_{r\theta}^{Res}. \quad (2)$$

The first term on the right-hand-side represents the diffusive stress due to turbulent momentum diffusion, i.e. turbulent viscous flux. χ_θ is the turbulent viscosity for poloidal flow. The second term represents the radial convection of poloidal momentum, and the third term is the residual stress, which has no leading dependence on $\langle v_\theta \rangle$ or $\partial \langle v_\theta \rangle / \partial r$. As a consequence of wave-flow momentum exchange, the residual stress drives an off-diagonal turbulent momentum flux, which is a function of the profiles of density and temperature (which drive the turbulence), i.e. $\Pi_{r\theta}^{Res} = \Pi_{r\theta}^{Res}(\nabla T, \nabla n)$, and of the turbulence intensity. The magnitude of residual stress scales with density gradient rather than temperature gradient in linear plasma devices, where the electron temperature is extremely low ($\sim eV$)[29]. Its divergence defines an intrinsic poloidal torque density[30], related to $\partial_r(\Pi_{r\theta}^{Res})$. Experimental measurement shows that, residual stress results from spectral asymmetry of the turbulence[31]. Note that $\Pi_{r\theta}^{Res}$ is a counterpart of the toroidal residual stress that drives intrinsic toroidal flow, which has been studied widely [32-42]. Here, we focus on the turbulent generation of edge poloidal flow.

Equation (3) follows from this decomposition. v_r^{eff} is ignored as it is negligible in the narrow edge shear layer [30, 43]. Note that both the viscous diffusive stress and residual stress contribute to the deviation of $\langle v_\theta \rangle$ from its neoclassical value, as shown in equation (3). Turbulence intensity gradients enter via $\partial_r \chi_\theta$ and $\partial_r(\Pi_{r\theta}^{Res})$.

$$\langle v_\theta \rangle - \langle v_\theta \rangle_{neo} = \frac{1}{\mu_{ii}^{(neo)}} \partial_r \left(\chi_\theta \frac{\partial \langle v_\theta \rangle}{\partial r} \right) - \frac{1}{\mu_{ii}^{(neo)}} \partial_r (\Pi_{r\theta}^{Res}) \quad (3)$$

The theory of rotation generation via turbulence effects is well developed. But direct experimental validation on tokamak plasmas is still incomplete. In this paper, the total Reynolds stress at the plasma edge is measured in Ohmic and ECRH heated L mode discharges.

Deviation of mean poloidal flow from its neoclassical value is derived. Analysis of fluctuation data is used to decompose the total stress into a turbulent viscous flux, which damps rotation, and a turbulent residual stress, which drives rotation. The dynamics of intrinsic poloidal torque dependence on spectral symmetry breaking is studied. We conclude with discussion of ongoing work and future directions.

The remainder of this paper is organized as follows: Section 2 introduces the experimental set up. Section 3 reports the relative deviation of poloidal rotation from neoclassical and the decomposition of Reynolds stress in Ohmic discharges. Section 4 reports the intrinsic poloidal torque and the broken symmetry of velocity fluctuations in L mode for different ECRH heating powers. Section 5 presents summary and conclusions.

2. EXPERIMENTAL SET UP

A specially designed Langmuir probe array on the outer mid-plane of the HL-2A tokamak was used to do the measurements, graphed by figure 1. The poloidal separation of adjacent tips is 6 mm, and the radial separation is 2.5mm, i.e. $d_\theta = 6\text{mm}$, $d_r = 2.5\text{mm}$. These are far less than the turbulent correlation length [44]. By using this probe, electron temperature, density, plasma velocities and Reynolds stress can be measured simultaneously. Verification of this kind of multi-step probe on plasma temperature, density and velocity measurement, and on turbulent transport measurement can be found in recent papers [45-47].

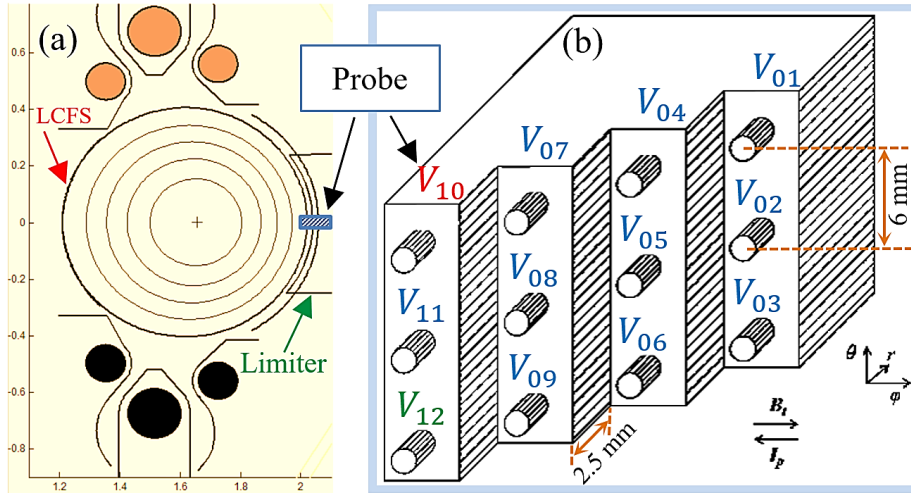


Figure 1. (a) The MHD equilibrium configuration reconstructed from EFIT; (b) Schematic diagram of Langmuir probe array on the outer mid-plane of HL-2A tokamak. $V_{10,+}$ and $V_{12,-}$ compose a double probe, combined with $V_{11,f}$ to form a triple probe. All the other channels are for floating potential measurements.

The fluctuating $E \times B$ radial velocity is inferred by the measured poloidal potential difference, $\tilde{v}_r = (\tilde{V}_{09,f} - \tilde{V}_{07,f})/2d_\theta B_\phi$. Similarly, fluctuating $E \times B$ poloidal velocity is inferred by the radial potential difference, $\tilde{v}_\theta = (\tilde{V}_{05,f} - \tilde{V}_{11,f})/2d_r B_\phi$. The poloidal velocity fluctuations are taken as $E \times B$ flow fluctuations. Hereafter, the orientation of a positive v_r is directed from core to vacuum chamber, and the orientation of a positive v_θ refers to the

electron diamagnetic direction. The turbulent Reynolds stress is computed as $\langle \tilde{v}_r \tilde{v}_\theta \rangle$, where $\langle \cdot \rangle$ indicates a time average. Plasma density can be inferred from ion saturation current $I_{sat} = (V_{10,+} - V_{12,-})/R_s$, where R_s is the shunt resistor that the ion current flows through. Electron temperature is inferred by $T_e = (V_{12,-} - V_{11,f})/\ln 2$. $T_i \sim T_e$ is assumed in the calculation of this paper. Combining ion saturation current and electron temperature, plasma density is inferred as $n_e = I_{sat}/(0.61eA_{eff}C_s)$, where C_s is the ion sound speed and A_{eff} is the effective current collection area. The particle flux is computed as $\langle \tilde{n}_e \tilde{v}_r \rangle$. In this study, a FIR digital filter was used to obtain the broadband fluctuation data with frequency 20-200 kHz.

The experiments are conducted in Ohmic and ECRH heated L mode deuterium discharges, in a limiter configuration on the HL-2A tokamak [48]. HL-2A is a medium-sized tokamak with a major radius of 1.65 m and a minor radius of 0.4 m. A typical ohmic discharge when experiments are conducted is shown in figure 2. The toroidal magnetic field is 1.35 T, the plasma current is 160 kA, the chord-averaged density is about $1.4 \times 10^{19} \text{ m}^{-3}$, and the stored energy is about 10.2 kJ. During 580-630 ms, the Langmuir probe moves into plasma with a constant velocity of 1 m/s. This process is marked by the orange rectangles in figure 2. This allows a radial profile measurement of the quantities. The position of last closed flux surface (LCFS) is set by the point where poloidal phase velocity of plasma fluctuations changes direction from the ion diamagnetic drift to electron diamagnetic drift [49, 50]. This is verified by the equilibrium configuration reconstruction from EFIT[51] within the error $\sim 2\text{mm}$. The depth that the probe shoots beyond LCFS can then be inferred. The plasma horizontal displacement in figure 2(d) is stable during the measurement. Z_{eff} for neoclassical velocity calculation is estimated by the visible bremsstrahlung diagnostic measurement[52].

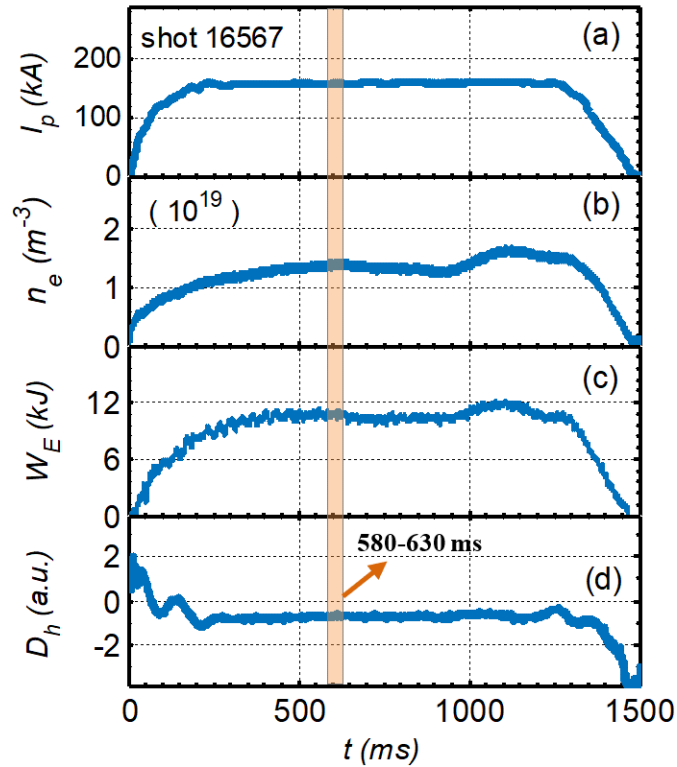


Figure 2. A typical ohmic discharge on the HL-2A tokamak: (a) plasma current; (b) central chord-averaged electron density; (c) stored energy; (d) plasma horizontal displacement.

From radial force balance equation, $v_{\theta i} = \nabla_r P_i / Z_i e n_i B_\phi - E_r / B_\phi + v_{\phi i} B_\theta / B_\phi$. Measurements of $v_{\theta, dia} = \nabla_r P_i / Z_i e n_i B_\phi$, $v_{\theta, E \times B} = -E_r / B_\phi$ and $v_{\theta, v_\phi} = v_{\phi i} B_\theta / B_\phi$ are all needed to infer $\langle v_\theta \rangle$. However, T_i and v_ϕ measurements are not available for these experiments. Given the limitation above, $v_{\theta, dia}$ is estimated by taking $T_i \sim T_e$ in Ohmic and L mode discharges for 400 kW and 700 kW ECRH. This gives $|v_{\theta, dia}| \sim 1.5$ km/s and $v_{\theta, dia} v_{\theta, E \times B} < 0$. Mach probe measurements from similar discharges gives $v_\phi \sim -10$ km/s. Along with B_θ / B_ϕ deduced from EFIT, $|v_{\theta, v_\phi}| \sim 1$ km/s and $v_{\theta, v_\phi} v_{\theta, E \times B} > 0$. $|v_{\theta, dia}|$ and $|v_{\theta, v_\phi}|$ are both less than $|v_{\theta, E \times B}|$ ($\sim 2-5$ km/s, as shown by figure 7(c)). $v_{\theta, dia}$ and v_{θ, v_ϕ} are of opposite sign and so tend to cancel in $\langle v_\theta \rangle$. Thus, the leading term, i.e. the $E \times B$ poloidal flow velocity is taken approximately as the mean poloidal flow velocity for these discharges, i.e. $\langle v_\theta \rangle \cong \langle v_{\theta, E \times B} \rangle$.

3. POLOIDAL ROTATION AND REYNOLDS STRESS IN OHMIC DISCHARGES

3.1. Rotation and its deviation from neoclassical

Neoclassical theoretical models for the calculation of poloidal rotation in tokamaks were proposed by Hazeltine[10], Hirshman-Sigmar[11], Kim-Diamond-Groebner[12] and Stacey-Sigmar[15]. Here, the KDG model is used for the calculation of neoclassical poloidal rotation for the main ion ‘‘i’’. $v_{\theta i, neo}$ is given by

$$v_{\theta i, neo} = \frac{B_\phi K^i T_i L_{T_i}^{-1}}{Z_i e B^2}. \quad (4)$$

Here, B_ϕ denotes toroidal magnetic field, viscosity ratio $K^i \equiv \mu_{01}^i / \mu_{00}^i$, T_i represents ion temperature and gradient scale length $L_{T_i}^{-1} \equiv -\ln T_i / dr$. Z_i is nuclear charge number, and B denotes magnetic field. The dimensionless collisionality is $\nu_i^* \equiv \nu_{ii} q R / (v_{thi} \varepsilon^{3/2}) \sim 1$, shown in Figure 3(a). Thus, we use plateau regime results for the calculation of $v_{\theta i, neo}$.

A significant deviation of the measured mean poloidal velocity from the neoclassical prediction in Ohmic discharges is observed, as shown by Figure 3(b). From equation (1), $\langle v_\theta \rangle - \langle v_\theta \rangle_{neo} = -\partial_r \langle \tilde{v}_r \tilde{v}_\theta \rangle / \mu_{ii}^{(neo)}$, where the neoclassical viscous damping rate $\mu_{ii}^{(neo)} = \varepsilon^2 \nu_{thi} / q R$, for the plateau regime [12] as shown in figure 3(d). The Reynolds stress in figure 3(c) has a negative divergence, giving a driving force in the electron diamagnetic direction. The role of turbulence on edge momentum rearrangement and sheared-flow development has been experimentally studied on different types of plasma devices [53-58]. Similar results have been observed on different devices, including the TEXTOR tokamak[57], TJ-IU[4] and TJ-II stellarator[58], linear plasma device CSDX[56] and Extrap-T2R[54] reversed field pinch experiments. Although the quantitative magnitude of $\langle \tilde{v}_r \tilde{v}_\theta \rangle$ differs in various devices (in the range of 10^5-10^8 m²/s²), the turbulent Reynolds stress consistently shows a notable negative radial gradient in the proximity of the edge velocity shear layer. This common feature may suggest a similar basic mechanism for turbulent generation of edge poloidal flow. The driving

force in the electron diamagnetic direction is consistent with the velocity shift towards the electron diamagnetic direction. The relative deviation (RD) of poloidal rotation from the neoclassical prediction due to turbulent Reynolds stress and neoclassical viscosity is then given by $RD = (-\partial_r \langle \tilde{v}_r \tilde{v}_\theta \rangle) / (\mu_{ii}^{(neo)} \langle v_\theta \rangle_{neo})$, as shown by the blue curve in figure 3(e). A direct calculation of relative deviation $(\langle v_\theta \rangle_{E \times B} - \langle v_\theta \rangle_{neo}) / \langle v_\theta \rangle_{neo}$ is shown by the red curve. The results by these two methods are both ~ 1.5 and of a similar trend. This indicates that the experimental measurement and theoretical model are in agreement. The experimental results suggest that the turbulent Reynolds stress and neoclassical viscosity are the mechanism responsible for the deviation of poloidal velocity from neoclassical. The result is semi-quantitatively coincident with the theoretical model[26].

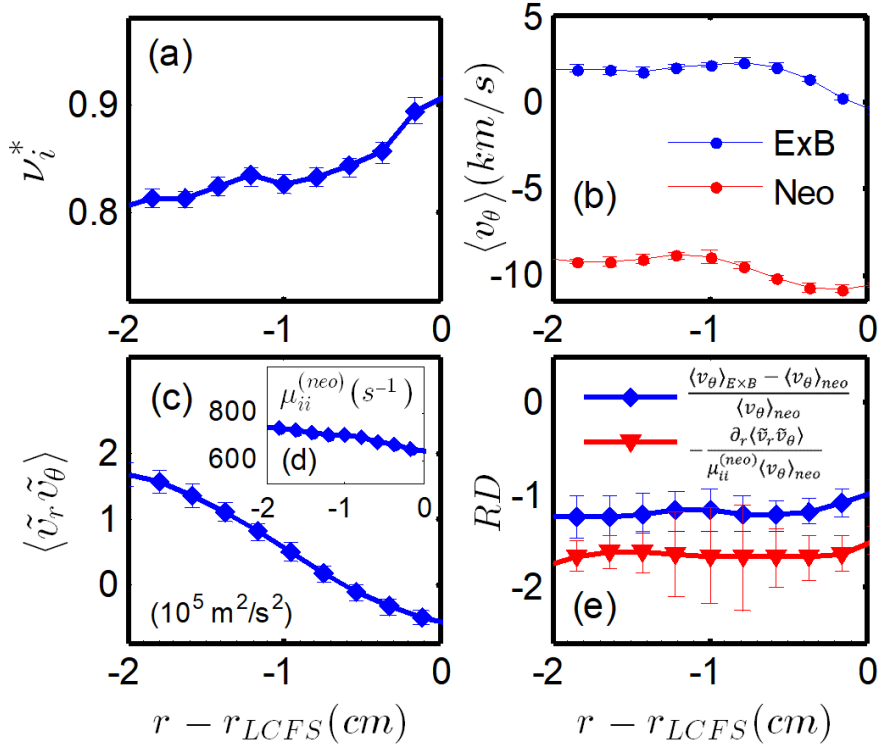


Figure 3. (a) Dimensionless collisionality v_i^* ; (b) Neoclassical poloidal velocity and experimentally measured $E \times B$ flow velocity; (c) turbulent Reynolds stress; (d) neoclassical viscosity $\mu_{ii}^{(neo)}$; (e) Relative deviation of poloidal rotation from neoclassical.

3.2. Decomposition of Reynolds stress

As we discuss in Sec. 1, the Reynolds stress can be decomposed into three terms. These are turbulent viscous flux, convection and residual stress, respectively. It's of natural interest to look for the contribution of these diffusive or non-diffusive stresses to the turbulent generation of poloidal flows. The pinch velocity in convection term is assessed by gyro-kinetic calculations [43], $v_r^{eff} \cong \chi_\theta / R$. Results indicate that, the convection term contributes little to rotation generation in the narrow edge shear layer. When compared to viscous diffusion in the strong shear layer of the plasma edge, it's weak and thus eventually neglected. Stationarity of the $E \times B$ flow and fluctuations can then be used to synthesize the turbulent viscosity from

fluctuation data. Combined with the measurement of the Reynolds stress, the residual stress can then be estimated [59].

The quasilinear expression for the ion flow diffusion coefficient (i.e. turbulent viscosity) is $\chi_\theta = \sum \frac{\langle \tilde{v}_r^2 \rangle |\gamma|}{(\omega - k_\theta v_\theta)^2 + |\gamma|^2}$, where the wave-particle decorrelation rate is $|\gamma| \sim \frac{1}{\tau_c}$, and τ_c is the decorrelation time. For modest turbulence, the spectral width exceeds the resonance width in χ_θ , so $\chi_\theta = \sum \langle \tilde{v}_r^2 \rangle \tau_{ac}$. Here, τ_{ac} is the spectral auto-correlation time. In general, $\tau_{ac} \leq \tau_c$, because τ_{ac} is spectrally integrated while τ_c is defined for each mode. Eddy-like structures exist in the edge shear layer. These persist on average for an auto-correlation time τ_{ac} . τ_{ac} is determined from the e-folding width of the temporal auto-correlation function of \tilde{v}_r fluctuations. The turbulent momentum diffusion coefficient χ_θ can be expressed in terms of the eddy radial velocity and the eddy auto-correlation time, via the relation $\chi_\theta = \langle \tilde{v}_r^2 \rangle \tau_{ac}$. The turbulent particle diffusion coefficient is D_n , which can be measured directly via $-\langle \tilde{n} \tilde{v}_r \rangle / \partial_r \langle n \rangle$. Figure 4 shows a plot of these two turbulent diffusivities. They are comparable and exhibit a similar trend. This is to be expected when the edge turbulence is electrostatic, which it is in the cases we consider. This consequence suggests that the synthesis of χ_θ gives a plausible result.

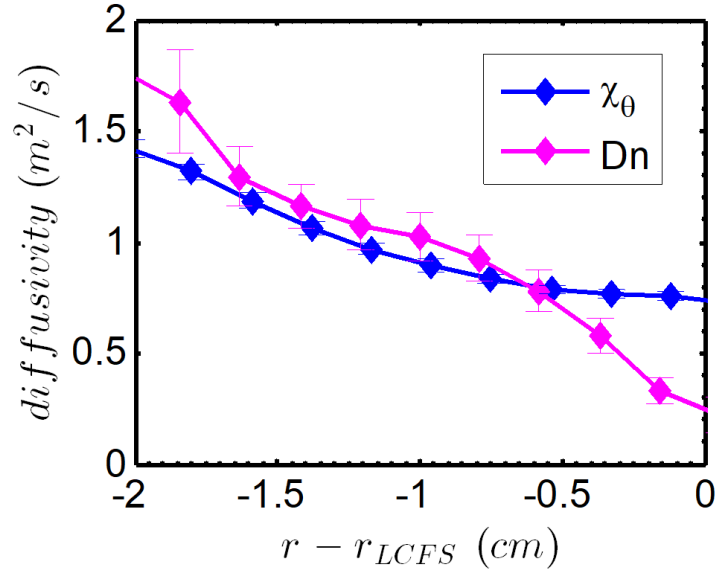


Figure 4. Comparison of turbulent momentum viscosity χ_θ to turbulent particle diffusivity D_n .

Using the turbulent momentum viscosity χ_θ , the $E \times B$ flow profile and the stationarity of the mean $E \times B$ flow, the diffusive stress can be synthesized via $-\chi_\theta \partial \langle v_\theta \rangle / \partial r$. The residual stress is then deduced by extracting the diffusive stress from the Reynolds stress, following the approach of references [31, 59]. In brief, the method is to directly measure the Reynolds stress and then to subtract off the diffusive flux, synthesized by direct measurement of turbulent intensity $\langle \tilde{v}_r^2 \rangle$, auto-correlation time τ_{ac} , and flow shear $\partial \langle v_\theta \rangle / \partial r$. The results are shown in Figure 5. Figure 5(a) shows the mean electron temperature and density profile in the region $r - r_{LCFS} = -2 - 0$ cm. Both of them have a strong gradient in the plasma edge. Figure 5(e) is the measured $E \times B$ poloidal velocity, and Figure 5(f) is the measured turbulent Reynolds stress. Figure 5(b)-(d) are the mean square of $E \times B$ radial velocity fluctuations, the

auto-correlation time of \tilde{v}_r , and the poloidal velocity shear, respectively. They are used to synthesize turbulent diffusive stress in figure 5(g). The calculated residual stress is shown by figure 5(h). Note that there exists a finite residual stress in the plasma edge. It's of the same order of magnitude as the diffusive stress. The residual stress has a strongly negative gradient in the edge region, which corresponds to a positive poloidal intrinsic torque, as a consequence of wave-flow momentum exchange. High torque exists in the strong shear layer $r - r_{LCFS} = -1 - 0$ cm. As turbulent viscous diffusion can only relax the neoclassical gradient and so acts to oppose the net rotation, this torque converts free energy (i.e. $\nabla T, \nabla n$)—accessed by the turbulence—to the drive of poloidal rotation and so subverts it from neoclassical[60].

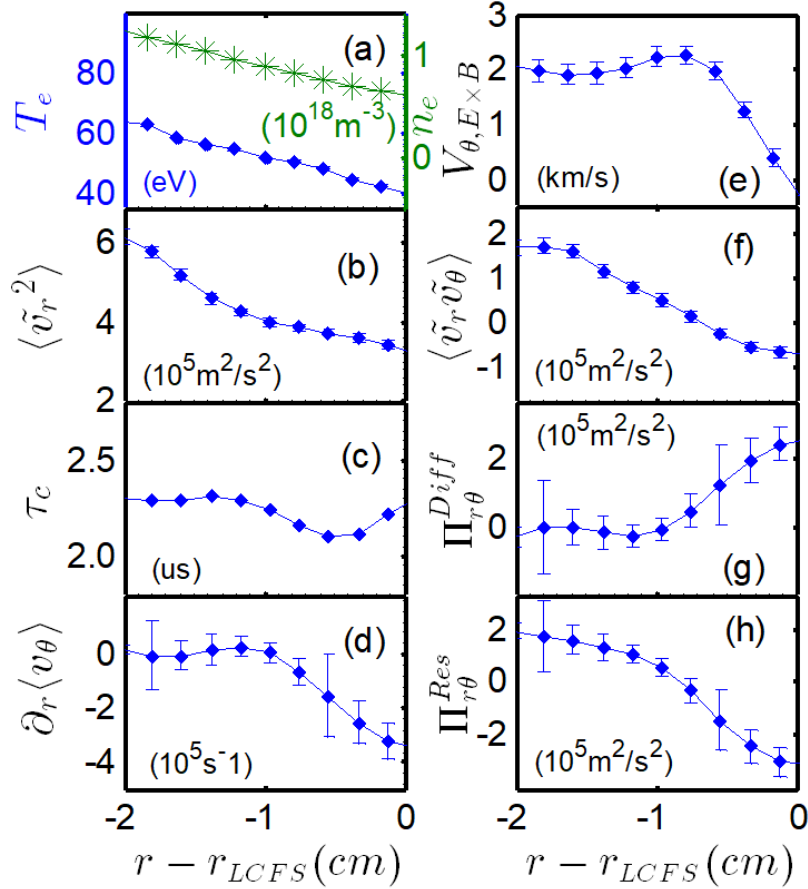


Figure 5. Decomposition of Reynolds stress. (a) Electron temperature and density; (b) mean square of $E \times B$ radial velocity fluctuations $\langle \tilde{v}_r^2 \rangle$; (c) auto-correlation time of \tilde{v}_r ; (d) velocity shear $\partial(v_\theta)/\partial r$; (e) $E \times B$ poloidal velocity; (f) Reynolds stress; (g) turbulent viscous flux, i.e. diffusive stress; (h) residual stress.

4. POLOIDAL ROTATION AND REYNOLDS STRESS IN L MODE FOR DIFFERENT ECRH POWERS

4.1. Rotation deviation from neoclassical and Reynolds stress

Since the turbulent flux converts free energy (i.e. $\nabla T, \nabla n$)—accessed by the turbulence—to drive poloidal rotation, similar studies have been done in L mode for different ECRH powers. Figure 6 shows the Reynolds stress and the relative deviation of poloidal rotation from

neoclassical $RD = (-\partial_r \langle \tilde{v}_r \tilde{v}_\theta \rangle) / (\mu_{ii}^{(neo)} \langle v_\theta \rangle_{neo})$ for 0/400/700kW ECRH heating power. As ECRH power increases, the neoclassical viscosity $\mu_{ii}^{(neo)}$ in figure 6(a) increases, and the slope of Reynolds stress in figure 6(c) obviously increases. Meanwhile, the relative deviation of poloidal rotation in figure 6(d) increases significantly. This suggests that the increased heating power leads to increased turbulence drive for the shear flow at the edge of the plasma.

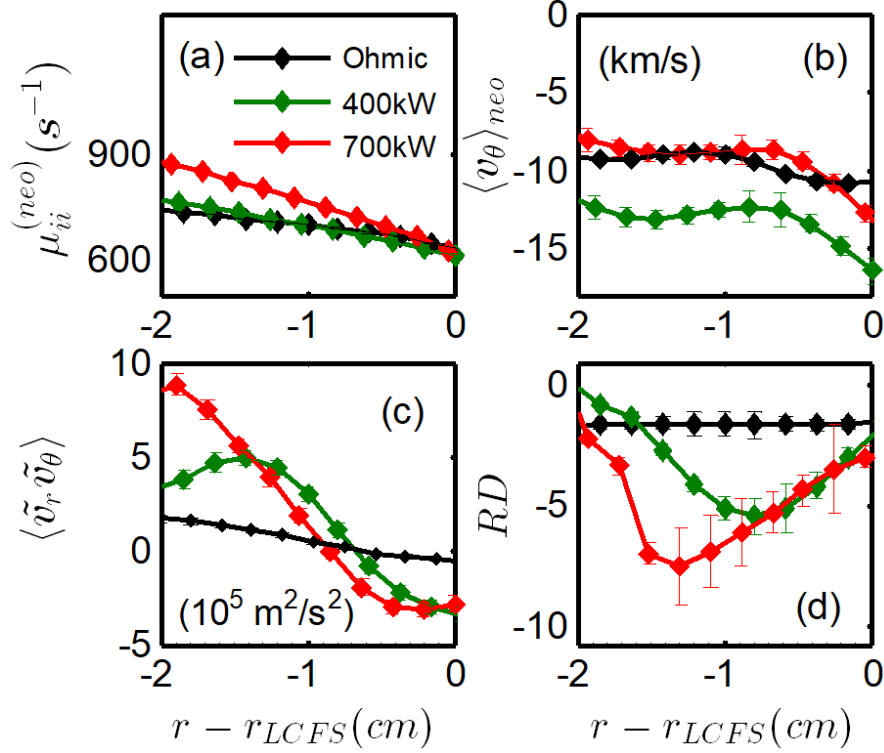


Figure 6. (a) neoclassical viscosity; (b) Neoclassical poloidal velocity; (c) turbulent Reynolds stress; (d) Relative deviation of poloidal rotation from neoclassical $RD = (-\partial_r \langle \tilde{v}_r \tilde{v}_\theta \rangle) / (\mu_{ii}^{(neo)} \langle v_\theta \rangle_{neo})$; in Ohmic and L mode discharges for 400 kW and 700 kW ECRH.

4.2. Intrinsic poloidal torque and broken symmetry

Figure 7(a) and figure 7(b) show the local electron temperature and density profile in Ohmic and 400/700 kW ECRH heated L mode discharges. Figure 7(c) represents the measured $E \times B$ poloidal velocity. Figure 7(d) gives the intrinsic poloidal torque $-\partial_r (\Pi_{r\theta}^{Res})$. With ECRH, temperature increases significantly, while density doesn't change much. As ECRH power increases, the intrinsic poloidal torque increases significantly and the region of torque extends inwards, thus driving an increasing poloidal flow. This is consistent with the increasing relative deviation of poloidal rotation from neoclassical, shown in figure 6(d). The physical process where gradients drive rotation via residual stress can be understood by considering the analogy with a car engine that burns fuel and converts thermal energy into kinetic energy of a rotating wheel[61]. In the framework of residual stress, the generation process of flows can be understood as a conversion of thermal energy, which is injected into a system by heating, into

kinetic energy of macroscopic flow by drift wave turbulence excited by ∇T , ∇n , etc, with broken symmetry.

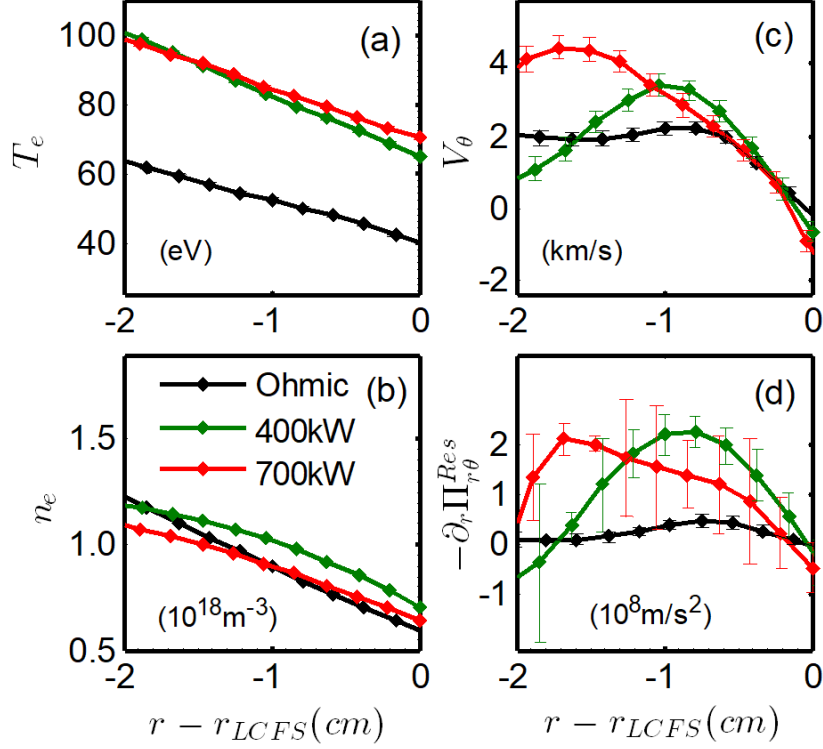


Figure 7. (a) Electron temperature; (b) electron density; (c) $E \times B$ poloidal rotation; (d) poloidal torque.

Since the residual stress drives an off-diagonal turbulent momentum flux, the development of the poloidal torque results from the broken symmetry in spectra of turbulence. This can be assessed by the joint probability distribution function (joint PDF) of radial and poloidal velocity fluctuations. Figure 8 shows the joint PDF of \tilde{v}_r and \tilde{v}_θ for Ohmic and 400/700 ECRH power cases at $r - r_{LCFS} = -1.0$ cm and $r - r_{LCFS} = -1.7$ cm. The joint PDF spectra of ECRH cases are much broader and more tilted than those of Ohmic. This corresponds to the development of larger turbulence intensity and increasing asymmetry. Note that, at the position -1.0 cm, the joint PDF for 400 kW ECRH tilts more to the first and third quadrants than the other two cases, as shown in figure 8(a)(b)(c). At this position, the poloidal torque for 400kW ECRH in figure 7(d) peaks. Besides, at the position -1.7 cm where the poloidal torque for 700 kW ECRH peaks, the joint PDF tilt is larger, as shown in figure 8(f). The elongation of the PDF in the radial direction for 400 kW ECRH at -1.7 cm (in figure 8(e)) may be caused by the reversal of poloidal $E \times B$ flow shearing in figure 7(c).

Combining the results above, the physical process of the turbulent generation of edge poloidal flows in tokamak plasmas is demonstrated experimentally. With injection of heating power, the turbulent stress more efficiently taps the free energy source (pressure gradient), and a finite residual stress develops from the spectral symmetry breaking in drift wave turbulence. These lead to profile relaxation and ultimately the generation of poloidal flow.

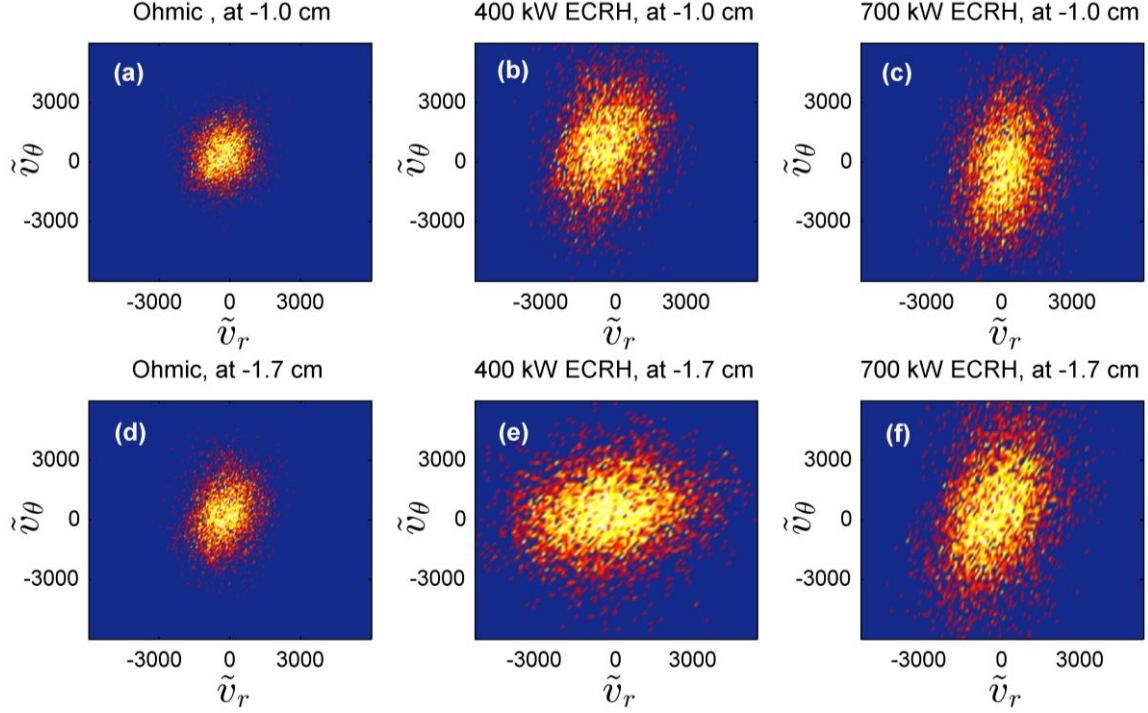


Figure 8. The joint PDF of radial and poloidal velocity fluctuations in Ohmic and 400/700 kW ECRH heated discharges at 1.0 cm and 1.7 cm inside LCFS.

5. SUMMARY AND CONCLUSIONS

This paper explores aspects of the physics of turbulent transport of poloidal momentum, and its impact on the mean flow by a multi-step Langmuir probe in HL-2A tokamak ohmic and L mode discharges. The principle results are:

- (a) The edge fluctuations, Reynolds stress and mean $E \times B$ flow are characterized.
- (b) Significant deviation of mean poloidal flow from the neoclassical value is deduced. This deviation increases with ECRH heating power. Both diffusive and non-diffusive stresses contribute to the deviation.
- (c) The turbulent poloidal viscous flux and residual stress are synthesized using fluctuation data. The turbulent poloidal viscosity is found to be comparable to the turbulent particle diffusivity.
- (d) The residual stress increases with heating power and manifests a sharper gradient at higher powers.
- (e) The joint PDF spectra of Reynolds stress in ECRH L mode discharges are much broader and more tilted than those from Ohmic plasmas. At the position where the poloidal torque (given by the divergence of the residual stress) peaks, the joint PDF tilts further. The broken symmetry of the turbulence spectra provides a good explanation for the development of poloidal torque in these experiments.

Taken together, the physical process of turbulent generation of edge poloidal flows in the tokamak can be deduced. With heating power injection, turbulence taps the free energy sources (i.e. pressure gradient), and a finite turbulent residual stress develops due to spectral symmetry

breaking in drift wave turbulence. These lead to profile relaxation and the generation of poloidal flow.

A limitation of this work is that the results discussed here are only from Ohmic and L-mode discharges. The inclusion of results from H-mode is desirable, because of the improved confinement performance of H-mode operation. Unfortunately, Langmuir probe measurements of Reynolds stress profile in H-mode of HL-2A tokamak are not available due to the effects of ELMs. Other diagnostics for Reynolds stress measurements are not yet fully functional. Thus, studies of Reynolds Stress and the turbulent generation of edge poloidal flows in H mode plasmas are postponed to future work. Besides, the ion temperature profile at the edge of HL-2A tokamak in non-NBI discharges is not available to be measured with existing diagnostics. $T_i \sim T_e$ is assumed in the calculation of this paper. The impact of the non-equality between the ion and electron temperature on the estimation of the deviation of the mean poloidal velocity from the neoclassical value should be explored in future.

Future work will focus on the investigation of phase dynamics for edge Reynolds stress and its effects on the turbulent generation of plasma flows. In particular, physics of the symmetry breaking in spectra of edge velocity fluctuations in Ohmic and L mode discharges strongly suggests a vital influence of the cross phase on turbulent generation of edge poloidal flows. A novel theoretical work indicates that, there exist two different states of the cross-phase: slipping and locked state in strong and weak shear regimes[62]. Relevant experimental study has shown an agreement with this theory by dividing the Reynolds stress directly into fluctuation, cross phase and coherence[49]. However, the “cross phase” between \tilde{v}_r and \tilde{v}_θ in the time domain contains the “coherence” information. The dynamics of cross phase and coherence in turbulent generation of plasma flows deserve further investigation. The studies of statistics of the probability distribution of cross phase are also planned for future work. Kurtosis--a measure of how fat the tail of the PDF is, skewness--a measure of the asymmetry and Hurst parameter--a measure of the correlation and memory in the dynamics, are strongly suggested for study in different flow regimes.

ACKNOWLEDGEMENTS

We have benefitted greatly from the First Chengdu Theory Festival 2018, where many relevant topics were discussed. We would also like to acknowledge discussions with Dr. Xuantong Ding, Prof. Zhen Yan and Dr. Rongjie Hong. This work is supported by National Key R&D Program of China under 2017YFE0300405, National Natural Science Foundation of China under Grant No. 11575055, 11875124, 11705052 and U1867222 and Chinese National Fusion Project for ITER under Grant No. 2015GB104000. The work is also supported by the U.S. Department of Energy, Office of Science, Office of Fusion Energy Sciences under Award Number DE-FG02-04ER54738.

REFERENCES

- [1] Kim, J., et al., *Physical Review Letters*, 1994. **72**(14): p. 2199-2202.
- [2] Burrell, K.H., *Physics of Plasmas*, 1997. **4**(5): p. 1499-1518.
- [3] Yan, Z., et al., *Physical review letters*, 2014. **112**(12): p. 125002.
- [4] Hidalgo, C., et al., *Plasma Physics and Controlled Fusion*, 2000. **42**(5A): p. A153-A160.
- [5] Ryter, F., et al., *Nuclear Fusion*, 2014. **54**(8): p. 083003.
- [6] Ryter, F., et al., *Plasma Physics and Controlled Fusion*, 2015. **58**(1): p. 014007.
- [7] Liang, A.S., et al., *Physics of Plasmas*, 2018. **25**(2): p. 022501.
- [8] Burrell, K.H., *Plasma Physics and Controlled Fusion*, 1994. **36**(7A): p. A291.
- [9] Bell, R.E., et al., *Physical Review Letters*, 1998. **81**(7): p. 1429-1432.
- [10] Hazeltine, R.D., *The Physics of Fluids*, 1974. **17**(5): p. 961-968.
- [11] Hirshman, S.P. and D.J. Sigmar, *Nuclear Fusion*, 1981. **21**(9): p. 1079.
- [12] Kim, Y.B., P.H. Diamond, and R.J. Groebner, *Physics of Fluids B: Plasma Physics*, 1991. **3**(8): p. 2050-2060.
- [13] Stacey, W.M., *Physics of Plasmas*, 2002. **9**(9): p. 3874-3883.
- [14] Solomon, W.M., et al., *Physics of Plasmas*, 2006. **13**(5): p. 056116.
- [15] Stacey, W.M., *Physics of Plasmas*, 2008. **15**(1): p. 012501.
- [16] Chrystal, C., et al., *Physics of Plasmas*, 2014. **21**(7): p. 072504.
- [17] Weston, M.S. and A.G. Brian, *Nuclear Fusion*, 2014. **54**(7): p. 073021.
- [18] Diamond, P.H. and Y.B. Kim, *Physics of Fluids B*, 1991. **3**(7): p. 1626-1633.
- [19] Biglari, H., P.H. Diamond, and P.W. Terry, *Physics of Fluids B*, 1990. **2**(1): p. 1-4.
- [20] Shaing, K.C. and E.C. Crume, *Physical Review Letters*, 1989. **63**(21): p. 2369-2372.
- [21] Hidalgo, C., et al., *Plasma Physics & Controlled Fusion*, 2006. **48**(4).
- [22] Yan, Z., et al., *Physics of Plasmas*, 2008. **15**(9): p. 092309.
- [23] Xu, M., et al., *Physical Review Letters*, 2011. **107**(5): p. 055003.
- [24] Tynan, G.R., et al., *Nuclear Fusion*, 2013. **53**(7): p. 073053.
- [25] Wang, L., et al., *Physics of Plasmas*, submitted. 2019.
- [26] McDevitt, C.J., et al., *Physics of Plasmas*, 2010. **17**(11): p. 112509.
- [27] Gürçan, Ö.D., et al., *Physics of Plasmas*, 2007. **14**(4): p. 042306.
- [28] Diamond, P., et al., *Physics of Plasmas (1994-present)*, 2008. **15**(1): p. 012303.
- [29] Hajjar, R.J., P.H. Diamond, and M.A. Malkov, *Physics of Plasmas*, 2018. **25**(6): p. 062306.
- [30] Diamond, P.H., et al., *Nuclear Fusion*, 2009. **49**(4): p. 571-576.
- [31] Hong, R., et al., *Physical Review Letters*, 2018. **120**(20): p. 205001.
- [32] Gonçalves, B., et al., *Physical Review Letters*, 2006. **96**(14): p. 145001.
- [33] Müller, S.H., et al., *Physical Review Letters*, 2011. **106**(11): p. 115001.
- [34] Wang, L. and P.H. Diamond, *Nuclear Fusion*, 2011. **51**(8): p. 083006.
- [35] Waltz, R.E., G.M. Staebler, and W.M. Solomon, *Physics of Plasmas*, 2011. **18**(4): p. 332-339.
- [36] Solomon, W.M., et al., *Nuclear Fusion*, 2011. **51**(7): p. 073010.
- [37] Xu, Y., et al., *Nuclear Fusion*, 2013. **53**(7): p. 072001.
- [38] Yue, S., et al., *Plasma Physics and Controlled Fusion*, 2014. **56**(1): p. 015001.
- [39] Li, J.C., et al., *Physics of Plasmas*, 2016. **23**(5): p. 052311.
- [40] Rice, J.E., *Plasma Physics and Controlled Fusion*, 2016. **58**(8): p. 083001.
- [41] Grierson, B.A., et al., *Physical Review Letters*, 2017. **118**(1): p. 015002.
- [42] Wang, W.X., et al., *Physics of Plasmas*, 2017. **24**(9): p. 092501.
- [43] Peeters, A.G., C. Angioni, and D. Strintzi, *Physical Review Letters*, 2007. **98**(26): p. 265003.
- [44] Zhao, K.J., et al., *Physical Review Letters*, 2006. **96**(25): p. 255004.
- [45] Nie, L., et al., *Nuclear Fusion*, 2018. **58**(3): p. 036021.
- [46] Jinbang, Y., et al., *Plasma Science and Technology* (accepted), 2019.
- [47] Ke, R., et al., *Journal of Instrumentation*, 2018. **13**(05): p. P05027-P05027.
- [48] Xu, M., et al., *Nuclear Fusion*, 2015. **55**(10): p. 104022.
- [49] Guo, D., et al., *Nuclear Fusion*, 2018. **58**(2): p. 026015.
- [50] Hong, R., et al., *Nuclear Fusion*, 2018. **58**(1): p. 016041.
- [51] Hongda, H., et al., *Plasma Science and Technology*, 2006. **8**(4): p. 397-401.
- [52] Liu, L., et al., *Fusion Engineering and Design*, 2019. **143**: p. 41-47.
- [53] Hidalgo, C., et al., *Physical Review E*, 2004. **70**(6): p. 067402.
- [54] Vianello, N., et al., *Physical Review Letters*, 2005. **94**(13): p. 135001.
- [55] van Milligen, B.P., et al., *Nuclear Fusion*, 2008. **48**(11): p. 115003.
- [56] Manz, P., et al., *Physics of Plasmas*, 2012. **19**(1): p. 012309.
- [57] Shesterikov, I., et al., *Physical Review Letters*, 2013. **111**(5): p. 055006.
- [58] Alonso, J.A., et al., *Plasma Physics and Controlled Fusion*, 2012. **55**(1): p. 014001.
- [59] Yan, Z., et al., *Physical Review Letters*, 2010. **104**(6): p. 065002.
- [60] Diamond, P.H., et al., *Nuclear Fusion*, 2013. **53**(10): p. 104019.
- [61] Kosuga, Y., P.H. Diamond, and Ö.D. Gürçan, *Physics of Plasmas*, 2010. **17**(10): p. 102313.
- [62] Guo, Z.B. and P.H. Diamond, *Physical Review Letters*, 2015. **114**(14): p. 145002.